

Research Article

Experimental Study on the Evolution Law of Mesofissure in Full Tailing Cemented Backfill

Yufan Feng , Guanghua Sun , Xuejian Liang , Chenyang Liu , and Yue Wang 

College of Mining Engineering, North China University of Science and Technology, Tangshan, Hebei 063210, China

Correspondence should be addressed to Guanghua Sun; czsgh110@163.com

Received 22 September 2020; Revised 22 October 2020; Accepted 24 October 2020; Published 10 November 2020

Academic Editor: Erol Yilmaz

Copyright © 2020 Yufan Feng et al. This is an open access article distributed under the Creative Commons Attribution License, which permits unrestricted use, distribution, and reproduction in any medium, provided the original work is properly cited.

To understand the mechanical properties of the backfill, to reveal the evolvement of micromechanical fissure of backfill, a uniaxial compression experiment was carried out for the full tailing cemented backfill. After loading, the microstructure of the specimens was observed by microscope and the pore characteristic parameters were analyzed. The results showed that the diameter of the initial damage hole of the backfill was mostly between 0 and 40 μm , the hole diameter increases gradually with the increase of pressure, and the hole diameter reached more than 5000 μm in the postpeak damage stage. The upper structure of the backfill specimen is compact while the lower structure is relatively loose. The cracks and interfaces between tailings particles and cement paste are mechanical weak surfaces, where the cracks are mainly generated and propagated. The tip of microfractures in the backfill is damaged by the influence of stress concentration. In the failure process, both surface porosity and fracture density decrease first and then increase, and the average pore diameter increases gradually. The results have guiding significance for the study of backfill mechanical properties and goaf filling design.

1. Introduction

The filling mining method uses tailings to fill goaf, which not only protects the mine surrounding environment but also reduces the discharge of tailings. Full tailing cemented backfill is an aggregate composed of tailings and cement cemented with different properties. Complex microscopic structures such as the size and composition of tailings, particles, structural surfaces, and microcracks directly affect the macroscopic mechanical properties, thus affecting the mine production safety. Therefore, it is helpful to understand the backfill mechanical properties and provide a certain basis for the safety of filling mining by exploring the mesofracture evolution law of backfill mesostructure.

Some scholars [1–4] have made great contributions to crack propagation and closure under uniaxial compression. Ghazvinian et al. [5] studied the thresholds for crack initiation (CI) and crack propagation (CD) in brittle rocks. Xue et al. [6] applied acoustic emission technology to study the damage stress threshold of different types of rock cracks under uniaxial compression. Rodriguez and Paola et al. [7]

studied fracture microcrack propagation in marble and pyromanganese ore by acoustic emission technology. Kumari et al. [8] used acoustic emission to study the corresponding fracture propagation patterns in the microstructure of rocks. Liu et al. [9] analyzed the failure mechanism of tailing cemented backfill with different gray-sand ratios and its mechanical properties under different ratios. Most of these studies are based on acoustic emission (AE). The temporal and spatial evolution of crack damage can be well described by AE technology, but the mesoscopic structure cannot be described in detail.

With the development of CT technology, it has been applied increasingly in geotechnical engineering. Ren et al. [10] analyzed the microcrack behavior between cement slurry and aggregate interface through CT. Shang et al. [11] and Hu and Yang [12] studied the relationship between rock porosity change and rock damage under uniaxial load by using nuclear magnetic resonance (NMR) to determine the porosity inside the rock. Zhang et al. [13] obtained the hole distribution of asphalt mixture by CT. Liang et al. [14] studied the internal void and aggregate distribution

characteristics of cement-stabilized macadam (CSM) through CT. Wang et al. [15, 16] proposed a Monte Carlo simulation method for the study of concrete microstructures and size effects and obtained the initiation and propagation of concrete microcracks. Kupwade-Patil et al. [17] used a variety of pore and microstructure characterization techniques such as X-ray and infrared spectroscopy to study the pore and microstructure of pozzolan in cement hardening. Sun et al. [18] conducted a real-time uniaxial compression scanning test using CT and a small loading device and discussed the pore evolution law during the bearing failure of cemented backfill (CPB). Through CT research, we can have a deeper understanding of the microscopic structure of rock and soil. Due to the limitations of CT images obtained through computer processing, the microstructure of backfill samples cannot be directly observed.

As conventional equipment for rock and ore identification in mineralogy and petrology, polarized light microscope is used to obtain two-dimensional petrographic photos of different scales. It can identify mineral particles with naked eyes and accurately quantify the structural characteristics of rocks with image processing and structural analysis software. Yang et al. [19] analyzed the structure and composition of granite. Higgins et al. [20] studied the volcanic activities of Quizapu and the cracks under the volcano through the analysis of andesite. O'Driscoll et al. [21] conducted an in-depth study on the genesis of the Bon Accord nickel deposit and believed that it might be related to the nickel oxide sulfide deposit related to the explosion of the Undersea Koma iron mine. Hepworth et al. [22] and Bradshaw [23] studied the origin of peridot crystals in peridot magma by observing a series of rock structures and geochemistry, respectively. Soulié et al. [24] studied the dissolution of magnesium-rich olivine at high temperature. Cheng et al. [25] discussed the source of potash feldspar crystal by analyzing the composition of the rhyolite in Emei Mountain. However, polarized light microscopy has rarely been reported in the field of mining and backfill research. Therefore, the microscopic images of backfill under uniaxial loading were observed by a polarized light microscope. The pore characteristic parameters and crack propagation forms of backfill were analyzed to understand the mechanical properties and reveal the mesofracture evolution law of backfill.

2. Test Design and Process

2.1. Sample Making. The aggregate was made of full tailings from an iron ore mine in Jidong, and the cementing agent was made of 42.5# Portland cement. The specimens with a concentration of 70% and a size of 200 mm × 200 mm × 200 mm were prepared according to a gray-sand ratio of 1:10 and maintained in the standard maintenance box for 28 days. The mechanical properties of the same batch of specimens are also different due to the influence of the size and composition of tailings particles and the structural surface between particles and microcracks. To ensure that the original damage structure and basic mechanical properties of the specimens are

consistent, the stability of the test results can be guaranteed to the greatest extent by taking the same specimen for testing. After curing, the use of core drilling in backfill specimen of nine $\Phi = 50$ mm core, according to sequence numbers 1~9 for use in subsequent tests. Then, polish the upper and lower ends of specimen nos. 1~8, leaving 100 mm in the middle. Specimen no. 9 was not polished for comparative analysis. The flowchart of sample preparation is shown in Figure 1.

2.2. Uniaxial Compression Test. The mechanical properties of the backfill at each stage of the loading process can be expressed by the stress-time curve. Therefore, in order to obtain the stress-time curve of the backfill under uniaxial loading, to divide the middle moment of the loading stage, uniaxial compression tests were carried out for the three specimens numbered 1~3 by uniaxial testing machine. To ensure full contact between the press and the sample, preloading was carried out before the test, with a limit of 10 kN and a moving speed of 2 mm/min. After the end of preloading, axial equivalent displacement loading was adopted with a loading rate of 0.15 mm/min. After the completion of the loading of specimen nos. 1~3, we obtain the stress-time curve as shown in Figure 2. The backfill loading stage is divided into compaction stage (stage I), elastic deformation stage (stage II), plastic deformation stage (stage III), and postpeak failure stage (stage IV) by dotted line. Find out the specific intermediate time corresponding to each stage as shown in Table 1. Stage 0 represents the raw specimen that has not been treated.

To study the evolution law of mesoscopic fracture in the whole loading, uniaxial loading test was carried out to obtain the failure of mesoscopic fracture at each stage. To maintain the initial damage of the backfill specimen and protect the original mesocrack, specimen no. 4 was not loaded. Then, specimens 5 to 8 were loaded according to the timetable in Table 1, respectively, and then the specimens were removed. The results of specimen treatment are shown in Table 2.

To facilitate the grease injection test and subsequent data analysis, specimens nos. 4~9 to be processed were renumbered first, and the numbering rules were shown in Table 3.

The first letter C represents the backfill, the second digit 10 represents the gray-sand ratio of 1:10, and the third digits 0, 1, 2, 3, and 4 represent the original specimen of the backfill, compaction stage, elastic deformation stage, plastic deformation stage, and postpeak failure stage, respectively. d stands for specimen no. 9 as the comparison specimen.

2.3. Vacuum Grease Injection Test. Thin section analysis can clearly observe the form and evolution process of mesocracks in each loading stage of the backfill. For this reason, BROU vacuum casting gauge in France was used to inject colored epoxy resin into the specimen. The principle is to pump the laboratory chamber into a vacuum and at the same time extract the air in the crack of the specimen. The resin enters into the crack to replace the air in the crack, to ensure that the cracks and pores in the specimen are not damaged

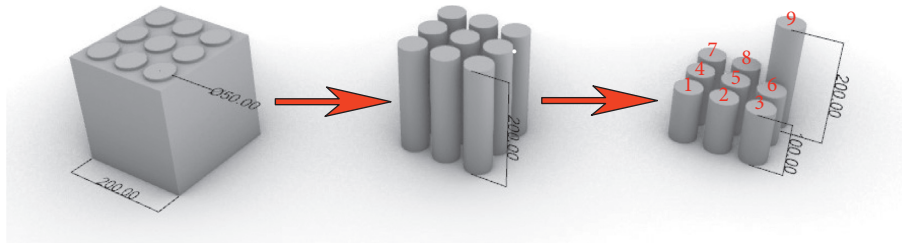


FIGURE 1: Schematic diagram for making backfill specimen.

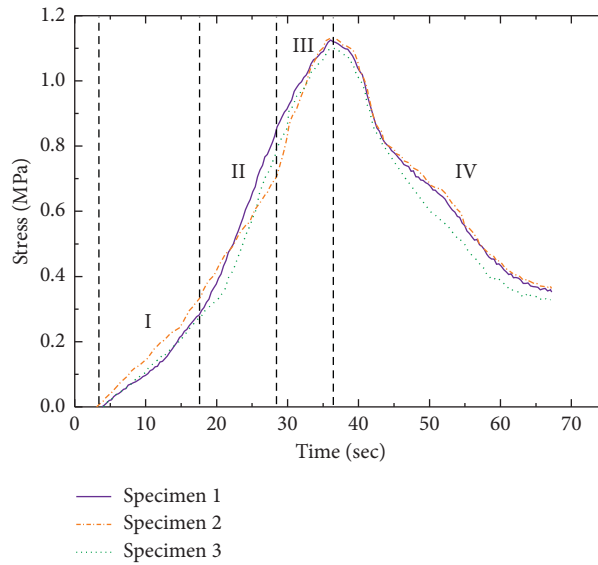


FIGURE 2: Stress-time curve of backfill under uniaxial compression.

TABLE 1: Intermediate schedule of backfill loading stage.

In the loading stage	Stage 0	Stage I	Stage II	Stage III	Stage IV
Intermediate time interval (sec)	0	10~12	23~25	32~33	50~60

TABLE 2: Treatment table of backfill specimen.

Specimen number	Take down the test piece time (sec)	In the loading stage
4	00	Original specimen
5	12	Compaction stage
6	24	Elastic deformation stage
7	33	Plastic deformation stage
8	55	Postpeak failure stage

TABLE 3: Number table of backfill.

Stratification	Number					
	4	5	6	7	8	9
Above	C-10-0-a	C-10-1-a	C-10-2-a	C-10-3-a	C-10-4-a	C-10-d-a
Middle	C-10-0-m	C-10-1-m	C-10-2-m	C-10-3-m	C-10-4-m	C-10-d-m
Below	C-10-0-b	C-10-1-b	C-10-2-b	C-10-3-b	C-10-4-b	C-10-d-b

during the grinding process and the morphology is preserved. Dyes are added to the resin to facilitate the resolution of solid particles and pores under a microscope under strong light.

First, the backfill was marked and stratified from top to bottom and put into the experimental chamber. Then the epoxy resin and curing agent were mixed at a ratio of 2 : 1, the catalyst and a small amount of blue dye were added, and

the evenly mixed glue solution was heated in a water bath at 80°C. After the system is vacuumed, the resin was injected into the laboratory, and samples were taken out and dried after pressurization. After drying, the samples were cut into cuboids with a size of 3 cm × 2 cm × 1 cm along the axial direction of the backfill and then ground into backfill casting slices with a thickness of 0.03 mm. A total of 18 backfill casting slices are made for slice analysis. See Figure 3 for the schematic diagram of test section making. Figure 4 shows the test process.

To ensure that the section would not affect the crack of the specimen during the test, first, the resin was injected after stratification to protect the crack inside the specimen from being destroyed. And then, the specimen is then cut after drying. At this point, any operation will not affect the cracks of the specimen, because the cracks are protected by resin. Finally, the reason why the blue part in the center of the specimen was selected for cutting was to avoid possible cracks in the stratification process, to ensure the accuracy of the test.

3. Test Results and Analysis

3.1. Evolution Characteristics of Mesoscopic Fissure. The “color image analysis system for pore characteristics and grain size of rock thin sections” developed by Sichuan University was used to process and calculate the parameters of the image of backfill cast thin sections obtained by Zeiss polarizing microscope, and then the pore distribution of backfill was quantitatively analyzed. The magnification of the image determines the number of microcracks observed in an image. If the multiple is too large, the microcracks are not complete. If the multiple is too small, the microcracks are not obvious in the image, and the image information will be lost during the image processing. To avoid this situation, the magnification is determined to be 100 times after comprehensive consideration. The middle position of the backfill was selected for observation and analysis of backfill casting thin section images. The gray part is the hardened set cement, the blue part is the dyed epoxy resin, and the others are tailing particles. The field of vision of the sample observed under the microscope is limited, and improper observation position will lead to errors in the analysis results. Therefore, images of the sample with typical characteristics are selected. To obtain enough microfracture information, the pore statistics are statistical histograms obtained from the same thin section based on multiple cross-section images.

(1) In the unloaded stage, the slice image and the histogram of pore statistics are shown in Figure 5. In Figure 5(a), it can be seen that there are already initial microcracks in the backfill. In Figure 5(b), the area frequency of hole diameter reaches the maximum in the range of 0~40 μm, and the cumulative area frequency is nearly 80%, indicating that there are a large number of microcracks and bubbles at the beginning, which constitute the initial damage of the backfill.

- (2) In the compaction stage, the slice image and the histogram of pore statistics are shown in Figure 6. In Figure 6(a), the backfill begins to be pressurized, the specimen is basically without infiltration of dyed epoxy resin, and the microcrack closes under pressure. In Figure 6(b), the frequency of the hole diameter area significantly disappears in the range of 40~60 μm and increases in the range of 20~40 μm, indicating that the microcrack and bubble in the filling are closed under pressure, and the specimen is in the compaction stage.
- (3) In the elastic deformation stage, the slice image and the histogram of pore statistics are shown in Figure 7. In Figure 7(a) the specimen was subjected to increased pressure, and the dyed epoxy resin entered the backfill and filled with microcracks, indicating that the backfill was reopened by the compaction cracks. The microcracks' tip was subjected to great concentrated stress, and the microcracks tip began to break. In Figure 7(b), the frequency of hole diameter area decreased in the range of 0~40 and increased in the range of, 40~100 μm, indicating that the crack gradually expanded at this stage.
- (4) In the plastic deformation stage, the slice image and the histogram of pore statistics are shown in Figure 8. In Figure 8(a), as can be seen from the area occupied by the epoxy resin (the blue part in the figure), the microcracks develop into larger cracks, while the contact part between the two cracks produces microcracks but does not connect. In Figure 8(b), the frequency of the hole diameter area significantly increases further, reaches more than 160 μm.
- (5) In the postpeak failure stage, the slice image and the histogram of pore statistics are shown in Figure 9. In Figure 9(a), in the postpeak failure stage, the backfill has clearly produced the through crack. In Figure 9(b), the frequency of hole diameter area increases between 180 and 200 μm. The through crack reduces the strength of the backfill, and the proportion above 5000 μm increases sharply, indicating that the macrocrack has been formed and the backfill has lost its bearing capacity after complete destruction.

The microcracks and bubbles constitute the initial damage of the backfill, which is mainly in the range of 0~40 μm. The 40~60 μm with large fissure was closed in the compaction stage, and with the increasing pressure, the reexpansion development increased from 40~100 μm to 160 μm to above 5000 μm. Therefore, a large number of microfractures are first distributed in the backfill. Under the action of pressure, some of these fractures expand and develop under pressure, leading to macroscopic failure of backfill. However, the stress of some fractures is not significant and the development of fractures is not obvious.

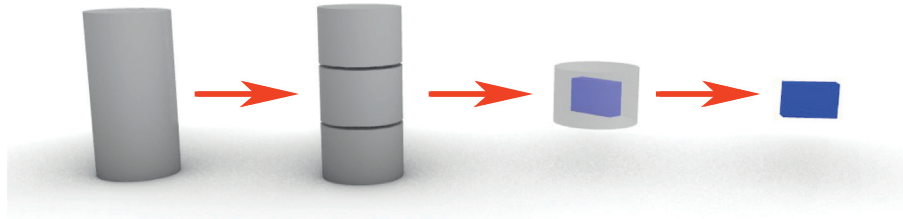


FIGURE 3: Schematic diagram of test slice cutting.

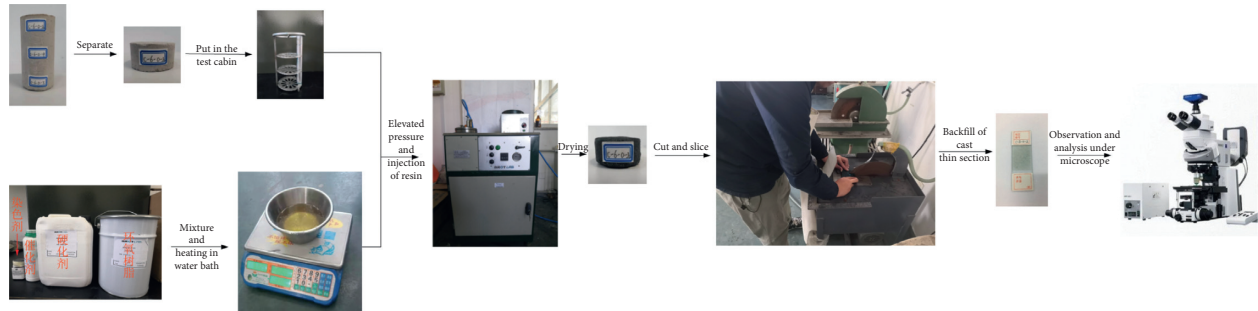
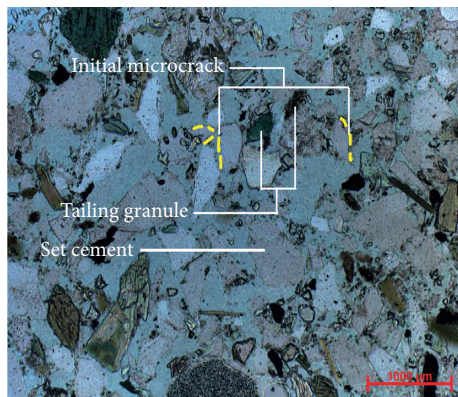
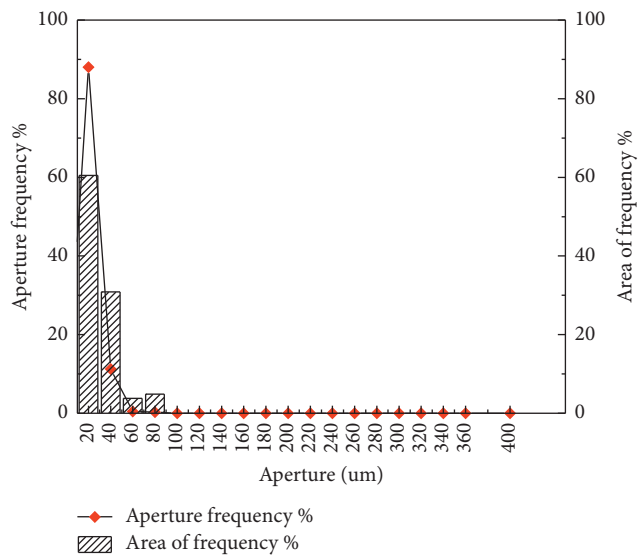


FIGURE 4: Flowchart of lipid injection test.



(a)



(b)

FIGURE 5: Original specimen of the cast thin section. (a) Slice image. (b) Pore statistical histogram.

3.2. *Characteristics of Backfill in the Direction of Gravity.*
 The filling slurry is uniform under ideal conditions without segregation and precipitation. However, segregation and settlement still exist in practice because of the fluidity of the filling slurry in the pipe. In addition, before the consolidation of filling slurry, the hydration reaction of cement has not been completely completed, and the consolidation force of cement on tailings particles is too weak. Figure 10 shows the upper, middle, and lower castings of the specimen with no. 9 backfill.

It can be seen from Figure 10(a) that there are many types of set cement and a large area. The upper layer of backfill is mostly cement with a tight structure. The lower layer, as shown in Figure 10(c), has more tailing particles and looser structure. As shown in Figure 10(b), the proportion of middle set cement and tailings particles is between the upper and lower layers. This phenomenon is obvious from the perspective of gravity analysis. Due to the different particle sizes of tailings, during the consolidation process of backfill, the coarsest particles firstly settle and accumulate in the

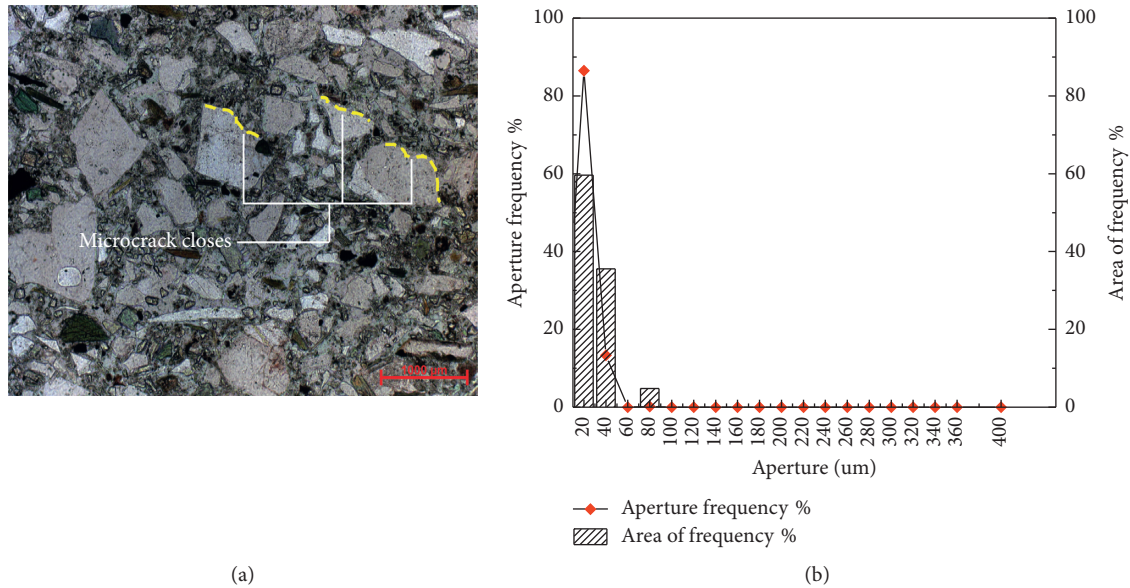


FIGURE 6: Compaction stage of the cast thin section. (a) Slice image. (b) Pore statistical histogram.

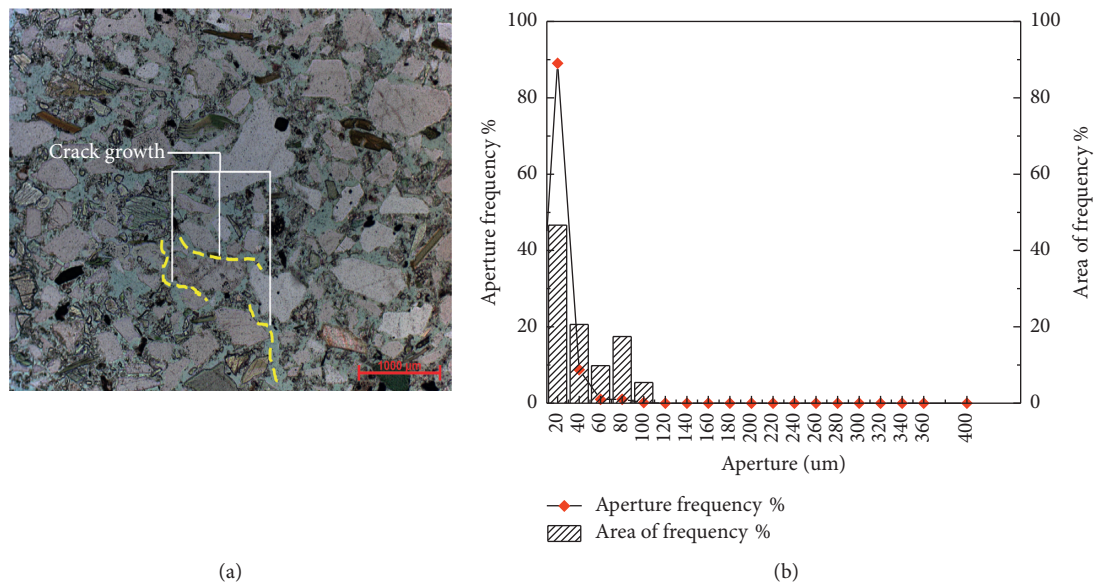


FIGURE 7: Elastic deformation stage of the cast thin section. (a) Slice image. (b) Pore statistical histogram.

lower end of backfill, while the unhydrated cement is on the upper layer of backfill. Therefore, this phenomenon will result in different mechanical strength of upper and lower ends of backfill under uniaxial compression. Therefore, in the pretreatment of Section 2.1 sample making, the upper and lower ends of the backfill were polished, the middle section is selected for the test, which reduces the influence to a certain extent, and the test results are more persuasive.

3.3. Propagation Law of Mesoscopic Fissure. To explore the propagation direction of mesoscopic fractures in the backfill, the cast slices of the backfill numbered "C-10-2-middle"

were observed under a microscope, and the picture shown in Figure 11 was obtained.

It can be clearly seen from the pictures that the microcracks in the backfill occur at the contact surface between tailing particles and set cement and are distributed and developed along the edge of tailing particles. Then, under the action of stress, the microcracks on the edge of the particles gradually develop and expand and then deflate and expand toward the cement stone area, finally forming the through cracks.

Under the action of pressure, the crack tip produces concentrated stress, which promotes the crack surface and microcrack propagation. The fracture and interface between

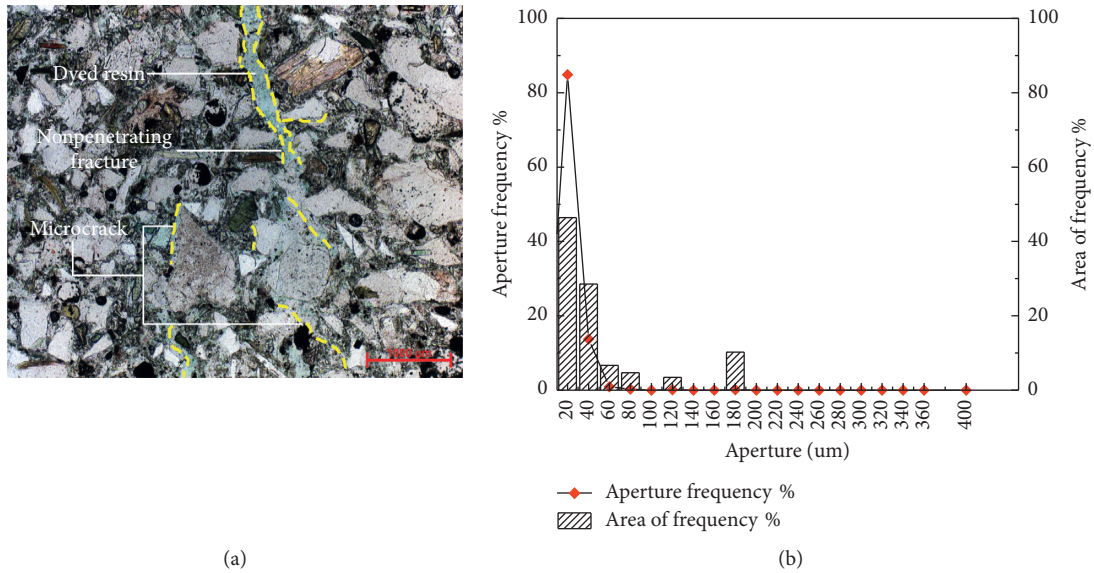


FIGURE 8: Plastic deformation stage of the cast thin section. (a) Slice image. (b) Pore statistical histogram.

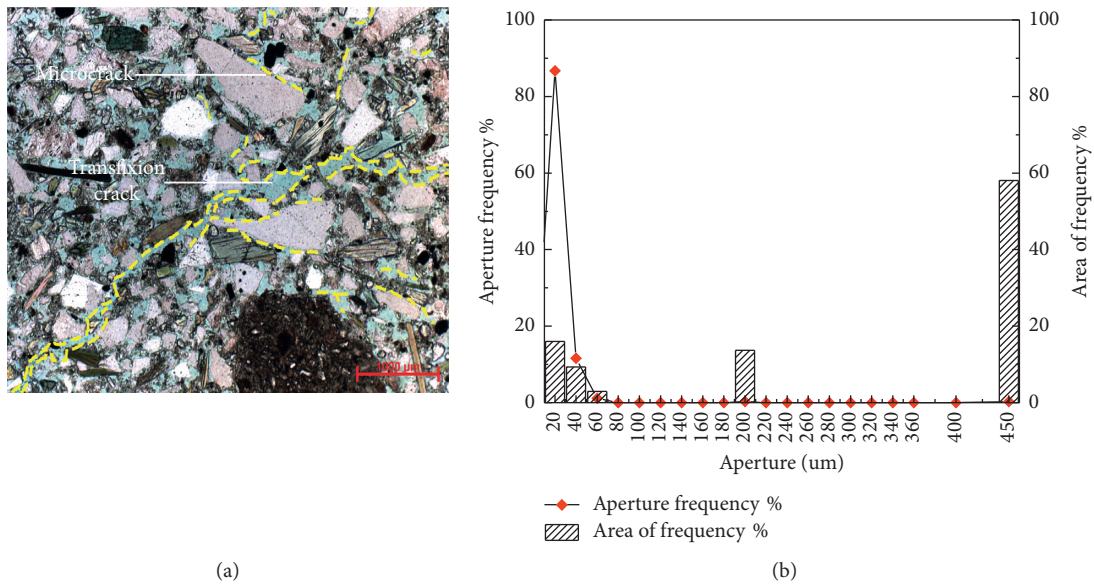


FIGURE 9: Postpeak failure stage of the cast thin section. (a) Slice image. (b) Pore statistical histogram.

tailing particles and set cement are the mechanical weak surfaces. This is because of their different hardness and the stress propagates at the interface between them. The difference in hardness leads to the formation of microcracks on the interface, which propagate on the interface and eventually develop into cracks throughout the backfill.

4. Discussion

As a composite material, full tailing cementing backfill is composed of full tailings, cement, water, bubbles, initial cracks, and so on. The early hydration slurries consist of

needles or sheets of fibers, which are not solid, but fine tubular and dendritic interlaced. Therefore, the backfill contains a large number of microcracks in a disorderly direction. Griffith failure criterion believes that there are many fine cracks in the material; under the action of force, the surrounding of these fine cracks, especially the crack end, can produce stress concentration phenomenon. Damage to the material often starts at the end of the crack and the crack spreads and eventually leads to complete damage to the material. The pore characteristic parameters of backfill under uniaxial loading are shown in Table 4.

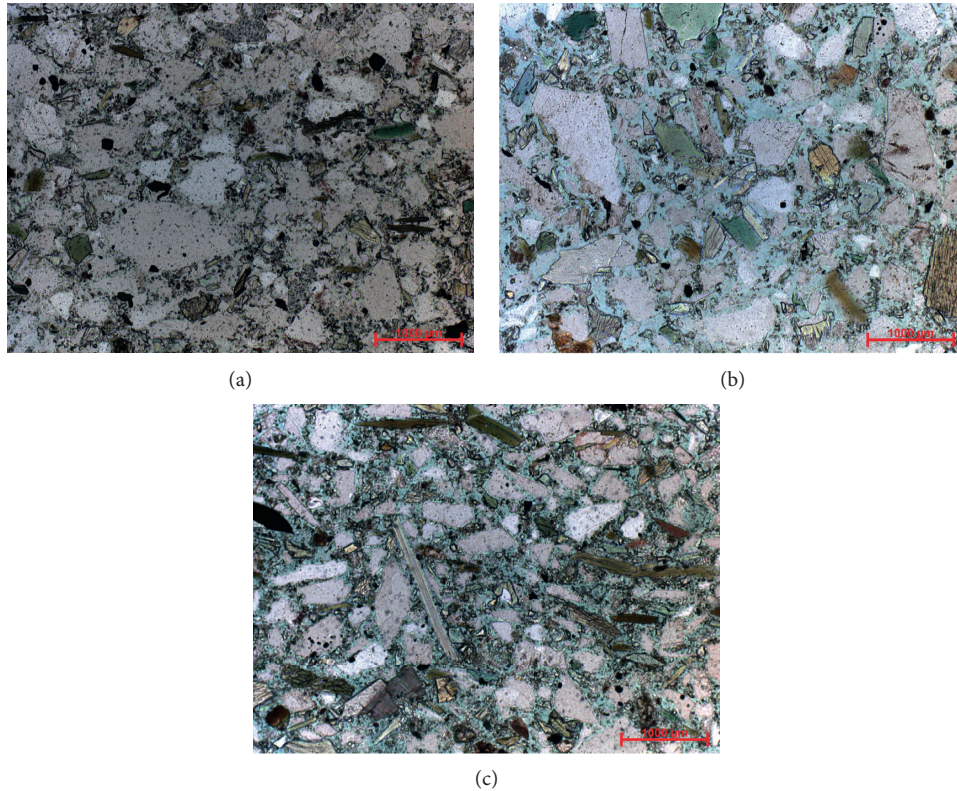


FIGURE 10: The cast thin slices in different positions of specimen no. 9. (a) C-10-d-above slice image (b) C-10-d-middle slice image. (c) C-10-d-below slice image.

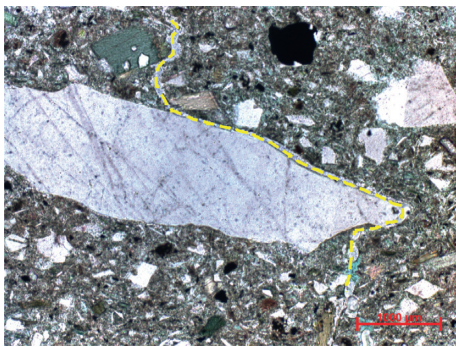


FIGURE 11: “C-10-2- middle” backfill casting thin section image.

Both the physics experiment of Chen et al. [26] and the simulation experiment of Xu et al. [27] show that cracks usually appear at the tip of cracks and then gradually expand around cracks. In their papers, they both mentioned that rock bridge (the rock mass between fractures that has not been penetrated), where the inner tip of the two fractures converge during the loading process, thus connecting the two fractures. Their research results and the research content of this paper can be well verified: in the elastic deformation stage, the fracture ends of microcracks begin to expand to the surrounding due to stress concentration; in the plastic deformation stage, the fracture is enlarged, but the fracture is not connected; it can be regarded as a “bridge” in the backfill. In the subsequent postpeak failure stage, the fracture is

connected. In this paper, the characteristics of crack evolution described by them are described in detail at different loading stages.

In the unloaded stage, the face rate and fracture density of the backfill are 8.77% and 2.32 mm/mm^2 , respectively, which are mainly the initial cracks formed on the interface between tailings particles and the set cement of the backfill and the undischarged bubbles. According to the Griffith failure criterion, it is assumed that the cracks are open and elliptically shaped and begin to crack at the tip edge wall of the open crack [28–31]. In the compaction stage, the backfill face rate and fracture density were reduced to 7.28% and 1.62 mm/mm^2 , respectively. The reason for the fracture closure of the backfill was that the compaction was worse than that of the rock. Under the action of external forces, the internal microcracks and bubble compression stress of the specimen led to compaction and closure, and the pore characteristic parameters were relatively reduced. In elastic deformation stage, face filling rate and fracture density were increased to 9.24%, 3.22 mm/mm^2 , with the increase of pressure, the microcracks after undergoes compression, new microcracks start to emerge at the seam end on the basis of the initial cracks, and the new cracks are mainly distributed between the tailing particles and the cement stone or around the larger tailing particles. In the plastic deformation stage, the face rate and fracture density of backfill increased significantly, which were 17.11% and 6.54 mm/mm^2 , respectively, indicating that the internal stress continued to increase, the cracks expanded rapidly, mainly along the edge

TABLE 4: Pore characteristic parameters of backfill.

In the loading stage	Face rate (%)	Characteristic parameter	
		Fracture density (mm/mm ²)	Average pore size (μm)
Original specimen	8.77	2.32	21.37
Compaction stage	7.28	1.62	22.05
Elastic deformation stage	9.24	3.22	34.53
Plastic deformation stage	17.11	6.54	42.54
Postpeak failure stage	25.44	14.66	266.41

of tailings particles to set cement, and a large number of microcracks were connected to form larger pores. In the postpeak failure stage, a large area of damage occurred inside the sample, and the face rate and fracture density of the backfill further increased, which were 25.44% and 14.66 mm/mm², respectively, indicating that the through crack had formed the bearing capacity of the macroscopic crack backfill. In summary, under uniaxial compression, the mesoscopic crack of the backfill body is damaged under the influence of tensile stress. However, the average pore size is increasing from 21.37 μm to 266.41 μm , indicating that the volume of the mesocrack of the backfill is increasing, the contact between tailings particles becomes less due to the propagation of cracks, the structure inside the specimen becomes loose, the cementing capacity of cement begins to decline, and the carrying capacity of the backfill decreases.

5. Conclusion

- (1) During the consolidation of backfill, due to the action of gravity, large tailings particles sink to the bottom, so the upper structure of consolidated backfill is compact, while the lower structure is relatively loose.
- (2) In the unloaded stage, the diameter of the initially damaged pores was mostly between 0 and 40 μm . With the increase of load, the diameter of the holes in the compaction stage decreased slightly, while the diameter of the holes in the elastic deformation stage increased in the range of 40~100 μm , and microcracks began to form and develop. In the plastic deformation stage, the diameter of the hole reaches more than 160 μm , and the crack expands rapidly. In the postpeak failure stage, the pore diameter is above 5000 μm , the crack is connected to the macrocrack, and the backfill is destroyed.
- (3) The fracture and interface of tailings particles and set cement are the weak mechanical surface and the weak position of the backfill. The generation and propagation of cracks mainly occur here.
- (4) In the failure process, the pore characteristic parameters, face rate and fracture density, both decrease first and then increase, and the average pore diameter gradually increases. The tip of the microcrack is destroyed by the influence of stress concentration, the crack volume increases gradually, the specimen structure becomes loose, and the carrying capacity of the backfill decreases.

Data Availability

All data, models, or codes generated or used during the study are available from the corresponding author or author upon request (Guanghua Sun, email:czsgh110@163.com).

Conflicts of Interest

The authors declare that there are no conflicts of interest regarding the publication of this paper.

Acknowledgments

This work was financially supported by the National Natural Science Foundation of China (51804122) and the Natural Science Foundation of Hebei (E2020209166).

References

- [1] C. H. Park and A. Bobet, "Crack initiation, propagation and coalescence from frictional flaws in uniaxial compression," *Engineering Fracture Mechanics*, vol. 77, no. 14, pp. 2727–2748, 2010.
- [2] P.-Q. Ji, X.-P. Zhang, and Q. Zhang, "A new method to model the non-linear crack closure behavior of rocks under uniaxial compression," *International Journal of Rock Mechanics and Mining Sciences*, vol. 112, 2018.
- [3] Y. Wang, X. Zhou, and Y. Shou, "The modeling of crack propagation and coalescence in rocks under uniaxial compression using the novel conjugated bond-based peridynamics," *International Journal of Mechanical Sciences*, vol. 128-129, pp. 614–643, 2017.
- [4] Y. Niu, X.-P. Zhou, and F. Berto, "Evaluation of fracture mode classification in flawed red sandstone under uniaxial compression," *Theoretical and Applied Fracture Mechanics*, vol. 107, Article ID 102528, 2020.
- [5] E. Ghazvinian, M. S. Diederichs, D. Labrie, and C. D. Martin, "An investigation on the fabric type dependency of the crack damage thresholds in brittle rocks," *Geotechnical and Geological Engineering*, vol. 33, no. 6, 2015.
- [6] L. Xue, S. Qin, Q. Sun, Y. Wang, M. Lee, and W. Li, "A study on crack damage stress thresholds of different rock types based on uniaxial compression tests," *Rock Mechanics and Rock Engineering*, vol. 47, no. 4, 2014.
- [7] P. Rodríguez, B. A. Paola, and T. B. Celestino, "Characterization of rock cracking patterns in diametral compression tests by acoustic emission and petrographic analysis," *International Journal of Rock Mechanics and Mining Sciences*, vol. 83, pp. 73–85, 2016.
- [8] W. G. P. Kumari, P. G. Ranjith, M. S. A. Perera, and B. K. Chen, "Experimental investigation of quenching effect on mechanical, microstructural and flow characteristics of

- reservoir rocks: thermal stimulation method for geothermal energy extraction,” *Journal of Petroleum Science and Engineering*, vol. 162, pp. 419–433, 2018.
- [9] Z.-x. Liu, M. Lan, S.-y. Xiao, and H.-q. Guo, “Damage failure of cemented backfill and its reasonable match with rock mass,” *Transactions of Nonferrous Metals Society of China*, vol. 25, no. 3, pp. 954–959, 2015.
- [10] W. Ren, Z. Yang, R. Sharma, C. Zhang, J. Philip, and Withers, “Two-dimensional X-ray CT image based meso-scale fracture modelling of concrete,” *Engineering Fracture Mechanics*, vol. 133, pp. 24–39, 2015.
- [11] J. Shang, J. Hu, K. Zhou, X. Luo, M. Mohammed, and Aliyu, “Porosity increment and strength degradation of low-porosity sedimentary rocks under different loading conditions,” *International Journal of Rock Mechanics and Mining Sciences*, vol. 75, 2015.
- [12] J.-H. Hu and D.-J. Yang, “Meso-damage evolution and mechanical characteristics of low-porosity sedimentary rocks under uniaxial compression,” *Transactions of Nonferrous Metals Society of China*, vol. 30, no. 4, pp. 1071–1077, 2020.
- [13] J. Zhang, J. Yang, T. Liu, R. Cai, and R. Yang, “Study on void structure reconstruction of asphalt mixture by X-ray computed tomography and otsu’s method,” *Advances in Materials Science and Engineering*, vol. 2020, Article ID 4546731, 13 pages, 2020.
- [14] C. Liang, Y. Wang, G. Tan, L. Zhang, Y. Zhang, and Z. Yu, “Analysis of internal structure of cement-stabilized macadam based on industrial CT scanning,” *Advances in Materials Science and Engineering*, vol. 2020, Article ID 5265243, 10 pages, 2020.
- [15] X. Wang, Z. Yang, P. Andrey, and Jivkov, “Monte Carlo simulations of mesoscale fracture of concrete with random aggregates and pores: a size effect study,” *Construction and Building Materials*, vol. 80, 2015.
- [16] X. Wang, M. Zhang, P. Andrey, and Jivkov, “Computational technology for analysis of 3D meso-structure effects on damage and failure of concrete,” *International Journal of Solids and Structures*, vol. 80, 2016.
- [17] K. Kupwade-Patil, S. D. Palkovic, B. Ali, C. Soriano, and O. Büyükoztürk, “Use of silica fume and natural volcanic ash as a replacement to Portland cement: micro and pore structural investigation using NMR, XRD, FTIR and X-ray microtomography,” *Construction and Building Materials*, vol. 158, pp. 574–590, 2018.
- [18] W. Sun, K. Hou, Z. Yang, and Y. Wen, “X-ray CT three-dimensional reconstruction and discrete element analysis of the cement paste backfill pore structure under uniaxial compression,” *Construction and Building Materials*, vol. 138, pp. 69–78, 2017.
- [19] Z.-F. Yang, Z.-H. Luo, X.-X. Lu et al., “The role of external fluid in the Shanggusi dynamic granitic magma system, East Qinling, China: quantitative integration of textural and chemical data,” *Lithos*, vol. 208–209, pp. 339–360, 2014.
- [20] M. Higgins, S. Voos, and A. J. Vander, “Magmatic processes under Quizapu volcano, Chile, identified from geochemical and textural studies,” *Contributions to Mineralogy and Petrology*, vol. 170, no. 5–6, pp. 1–16, 2015.
- [21] B. O’Driscoll, P. L. Clay, R. G. Cawthorn et al., “Trevorite: Ni-rich spinel formed by metasomatism and desulfurization processes at Bon Accord, South Africa?” *Mineralogical Magazine*, vol. 78, no. 1, pp. 145–163, 2014.
- [22] L. N. Hepworth, B. O’Driscoll, R. Gertisser, J. S. Daly, and C. H. Emeleus, “Incremental construction of the unit 10 peridotite, rum eastern layered intrusion, NW scotland,” *Journal of Petrology*, vol. 58, no. 1, pp. 137–166, 2017.
- [23] R. W. Bradshaw, A. J. R. Kent, and F. J. Tepley, “Chemical fingerprints and residence times of olivine in the 1959 Kilauea Iki eruption, Hawaii: insights into picrite formation,” *American Mineralogist*, vol. 103, no. 11, pp. 1812–1826, 2018.
- [24] C. Soulié, G. Libourel, and L. Tissandier, “Olivine dissolution in molten silicates: an experimental study with application to chondrule formation,” *Meteoritics & Planetary Science*, vol. 52, no. 2, 2017.
- [25] L.-L. Cheng, Y. Wang, J. S. Herrin, Z.-Y. Ren, and Z.-F. Yang, “Origin of K-feldspar megacrysts in rhyolites from the Emeishan large igneous province, southwest China,” *Lithos*, vol. 294–295, pp. 397–411, 2017.
- [26] M. Chen, H. Jing, X. Ma, H. Su, M. Du, and T. Zhu, “Fracture evolution characteristics of sandstone containing double fissures and a single circular hole under uniaxial compression,” *International Journal of Mining Science and Technology*, vol. 27, no. 3, pp. 499–505, 2017.
- [27] H. Xu, Y. Qin, G. Wang, C. Fan, M. Wu, and R. Wang, “Discrete element study on mesomechanical behavior of crack propagation in coal samples with two prefabricated fissures under biaxial compression,” *Powder Technology*, vol. 375, pp. 42–59, 2020.
- [28] B. Shen, T. Siren, and M. Rinne, “Modelling fracture propagation in anisotropic rock mass,” *Rock Mechanics and Rock Engineering*, vol. 48, no. 3, 2015.
- [29] W. Sun, A. Wu, K. Hou, Y. Yang, L. Liu, and Y. Wen, “Real-time observation of meso-fracture process in backfill body during mine subsidence using X-ray CT under uniaxial compressive conditions,” *Construction and Building Materials*, vol. 113, pp. 153–162, 2016.
- [30] J. Jin, P. Cao, Y. Chen, C. Pu, D. Mao, and X. Fan, “Influence of single flaw on the failure process and energy mechanics of rock-like material,” *Computers and Geotechnics*, vol. 86, 2017.
- [31] Y.-H. Huang, S.-Q. Yang, M. R. Hall, W.-L. Tian, and P.-F. Yin, “Experimental study on uniaxial mechanical properties and crack propagation in sandstone containing a single oval cavity,” *Archives of Civil and Mechanical Engineering*, vol. 18, no. 4, 2018.